Cement and Concrete Research 74 (2015) 1–9

Contents lists available at ScienceDirect

Cement and Concrete Research

journal homepage: http://ees.elsevier.com/CEMCON/default.asp

Application of gamma-ray radiography and gravimetric measurements after accelerated corrosion tests of steel embedded in mortar

Gustavo Duffó [a,b,c,*], Natalia Gaillard [c], Mario Mariscotti [d], Marcelo Ruffolo [d]

[a] Comisión Nacional de Energía Atómica, Gerencia Materiales, Depto. Corrosión, Av. Gral. Paz 1499, 1650 San Martín, Buenos Aires, Argentina
[b] Consejo Nacional de Investigaciones Científicas y Técnicas (CONICET), Av. Rivadavia 1917, 1033 Buenos Aires, Argentina
[c] Universidad Nacional de San Martín, Av. Gral. Paz 1499, 1650 San Martín, Buenos Aires, Argentina
[d] Tomografía de Hormigón Armado S.A. (THASA), Reclus 2017, 1609 Boulogne, Buenos Aires, Argentina

ARTICLE INFO

Article history:
Received 17 February 2014
Accepted 30 March 2015
Available online xxxx

Keywords:
Characterization (B)
Corrosion (C)
Electrochemical properties (C)
Reinforcement (D)
Mortar (E)

ABSTRACT

The accelerated corrosion by the impressed current technique is widely used in studies of concrete durability since it has the advantage that tests can be carried out within reasonable periods of time. In the present work the relationship between the applied current density and the resulting damage on the reinforcing steel, by applying optical microscopy, scanning electron microscopy, gamma-ray radiography and gravimetric measurements, was studied by means of the implementation of accelerated corrosion tests on reinforced mortar. The results show that the efficiency of the applied current is between 1 and 77%, regardless of the applied current density, the water/cement ratio and the mortar cover depth of the specimens. The results show the applicability of the gamma-ray radiography technique to detect localized corrosion of steel rebars in laboratory specimens.

1. Introduction

The corrosion of steel bars is the major cause of premature deterioration of reinforced concrete structures. Initially, due to the high alkalinity of the solution contained in the pores of the concrete (pH > 13), steel bars are passivated by the presence of a protective oxide film. However, under certain circumstances, this protection is broken by destruction of the passive film due to the presence of aggressive ions (chloride, for example) or by the acidification of the medium in the vicinity of the steel rods (carbonation) [1–3]. Under natural conditions, the corrosion process of reinforcing bars is very slow and usually the first signs of deterioration appear after many years of exposure, so the tests require long exposure times. Therefore, there is a tendency to perform what is called "accelerated corrosion tests", in order to obtain results in the short term. These tests can be performed applying a constant current density or a constant potential. After (or while) these tests are performed, it is necessary to determine or measure some outputs to establish relationships between the variables involved. Among these outputs, time-to-cracking, loss weight, stress–strain behaviour, etc. are the most frequently employed to evaluate the system [4–15]. However, in spite of the fact that several researches have been made on this subject, there is not a complete agreement concerning the effect of the different parameters on the results.

The objective of this work was to determine the effect of several variables such as the applied current density; the water/cement ratio and the mortar cover depth, on the efficiency of the accelerated corrosion test, evaluated by means of gravimetric test and gamma-ray radiography. Gamma rays have been employed to study the condition of concrete structures for more than five decades [16]. The extension of this application for locating steel reinforcing bars was proposed shortly after the first reports on the use of gamma rays in this field were published [17]. However, probably owing to the requirement of licences and the current social apprehension towards radiation, the interest for this particular non-destructive test (NDT) tool for civil engineering has until now been limited and has not been developed to its full potential. Gamma-ray radiography has the advantage over other techniques (i.e. X-ray radiography) that the radiation used is emitted spontaneously so that electrical power is not needed. This technique can be applied for non-destructive inspection and diagnosis of reinforced concrete structures with cleanliness and convenience. In spite of the fact that this technique has been applied for real structures, little information is found in the literature concerning its applications for basic studies on corrosion of reinforced concrete.

2. Experimental technique

The cement used was an ordinary Portland cement (OPC) with a chemical composition shown in Table 1 (the table also includes the total chloride content of the sand used). The sand/cement proportion used in this study was 3, while for studying the effect of the water/

* Corresponding author. Tel.: +54 11 6772 7403; fax: +54 11 6772 7388.
E-mail address: duffo@cnea.gov.ar (G. Duffó).

http://dx.doi.org/10.1016/j.cemconres.2015.03.017
0008-8846/

Table 1
Chemical composition of the cement, and chloride content of the sand used in the present work.

	% w/w
Cement	
Insoluble residue	3.22
Loss by calcination	11.10
Sulphur trioxide (SO_3)	2.00
Magnesium oxide (MgO)	1.24
Chloride (Cl^-)	0.06
Sulphide (S^{2-})	0.05
Silicon dioxide (SiO_2)	16.30
Calcium oxide (CaO)	56.96
Aluminium oxide (Al_2O_3)	4.26
Iron (III) oxide (Fe_2O_3)	4.02
Sodium oxide (Na_2O)	0.10
Potassium Oxide (K_2O)	0.69
Total alkaline ($Na_2O + 0.658K_2O$)	0.55
Sand	
Chloride (Cl^-)	0.08

cement (w/c) ratio, two proportions were used: (a) w/c = 0.5 and (b) w/c = 0.6.

The reinforcement was a 1040 carbon steel rod, 5 mm in diameter and 50 mm long. The chemical composition of the steel is shown in Table 2. After being polished with silicon carbide abrasive papers up to grade 600, rinsed with distilled water and degreased with ethyl acetate, the roads were weighted (up to 0.0001 g). Then the steel surface was coated with an electric insulator, except for a zone with an area of 4.6 cm^2. This uncoated area was embedded in the mortar.

A typical lollypop reinforced mortar test specimen was used. After mixing (according to ASTM C 305-11 standard) [18], the fresh mortar was poured into cylindrical plastic mould of 2 different sizes: 30 mm in diameter and 50 mm high in one case (specimens type A), and 71 mm in diameter and 50 high in the other (specimens type B), where the reinforcement was previously placed along its longitudinal axis (Fig. 1). So, the cover thickness of the specimen A was 12 mm, while for specimen B was 33 mm. The specimens were then compacted during 60 s by using a vibrating table and then they were stored at room temperature and 98% relative humidity (RH) during 28 days before testing. Several prismatic specimens (4 cm × 4 cm × 16 cm) were cast and stored as previously mentioned, in order to determine the mechanical properties of the mortars. The results are shown in Table 3.

For the accelerated corrosion tests, the working electrode is the steel bar embedded in mortar, to which the current is applied. The counter-electrode is a 316 stainless steel grid that is placed all around the cylindrical concrete. The specimens were then wrapped with a damp cloth. Previous to the tests, the mortar specimens were placed in a plastic container containing tap water (up to 400 mm height) for 24 h to ensure its complete wetting.

A power supply was used for applying a constant, direct current between the reinforcement and the counter-electrode. The rebar was connected to the positive pole of the power supply, and thus became anodic. The counter-electrode was connected to the negative pole.

Table 2
Chemical composition of the steel bars used in the present work.

Element	% w/w
C	0.36
Si	0.21
Mn	0.73
P	0.007
S	0.013
Cr	0.05
Ni	0.03
Mo	<0.01

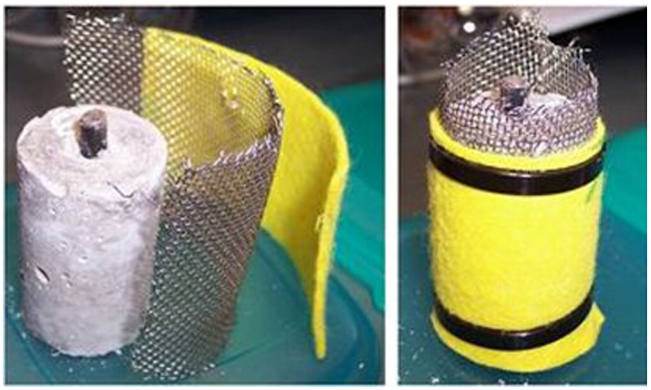

Fig. 1. Mortar specimen before (left) and after (right) wrapping a steel grid and a damp cloth around them.

Two or three specimens, kept in different containers, were connected in series for each set of experiences. The reinforcing steel was polarized by a constant current. Several levels of current density (i_{app}), between 50 μA/cm^2 and 750 μA/cm^2 were applied to accelerate the corrosion processes.

After finishing the tests (in most cases after 15 days), gamma-ray radiography was performed on the specimens. Gamma rays from a radioactive source (in the present work, a ^{137}Cs source that emits 0.67 MeV gamma rays was used) illuminate the specimens to be examined, and the transmitted beam is collected and turned into an image on a photographic film. The image obtained is in the form of a two-dimensional projection which provides information about the physical characteristics of the specimens. After that, the image was digitalized and an image analysis was performed using the Software Image J™. After calibrating the technique, a detection limit of 90 μm was determined.

After the gamma-ray radiography, the steel bars were removed from the mortar specimen and cleaned of rust using cleaning chemical procedures according to a standard [19] in order to obtain the weight loss produced by the accelerated corrosion test.

The theoretical mass of rust produced per unit surface area of the bar due to the applied current over a given time can be determined using the following expression based on Faraday's law:

$$M_{th} = \frac{i_{app} \cdot A \cdot t}{n \cdot F} \quad (1)$$

where M_{th} is the theoretical mass of rust per unit surface area of the bar (g/cm^2); i_{app} is the applied current density (A/cm^2), A is the atomic weight of iron (55 g/mol), t the duration of the induced corrosion (s); n is the valence of iron (2); and F is the Faraday's constant (96,487 Amp/mol).

The weight loss of steel per unit surface area and time (corrosion rate = CR) is determined by gravimetric tests in accordance with ASTM G1-90 standard performed on the steel bars extracted from the mortar by breaking the specimens after the accelerated corrosion test is completed:

$$CR = \frac{\left(W_f - W_i\right)}{\pi \cdot D \cdot L \cdot t} \quad (2)$$

Table 3
Mechanical properties of the mortar used in the present work, after 28 days curing at 98% relative humidity.

w/c	Flexural modulus (MPa)	Compressive strength (MPa)
0.5	4.0 ± 0.3	32 ± 5
0.6	3.5 ± 0.8	24 ± 2

where W_i is the initial weight of the bar before corrosion (g); W_f is the weight of the bar after corrosion (g) for a given duration of induced corrosion (t); D is the diameter of the rebar (cm); and L is the length of the rebar sample (cm).

Taking into account the weight loss, the effective corrosion current density (i_{eff}) can be determined with the following equation:

$$i_{eff} = \frac{CR \cdot n \cdot F}{A}. \quad (3)$$

Finally, the efficiency of the accelerated corrosion test (E_f) can be calculated as:

$$E_f = \frac{i_{eff}}{i_{apl}} * 100. \quad (4)$$

In another set of accelerated corrosion tests, samples were cut into slices and then ground with silicon carbide abrasive papers from grades 120 to 1000 lubricated with ethanol. The polishing with ethanol was performed in order to avoid modification of the rust layer during the sample preparation. The specimens so prepared were observed with an optical microscope (Olympus BX60M) as well as with a scanning electron microscope (Quanta 200). The corrosion product formed on the steel bars was manually scrapped and analysed by transmission Mossbauer spectroscopy (TMS). TMS was performed using a ^{57}Co source in a Rh matrix. Spectra were collected at room temperature (RT) and at 20 K using a He closed-cycle cryostat. Analysis of the spectra was performed using the Normos least-squares fitting programme [20]. Isomer shift values are given relative to α-Fe at room temperature.

Additionally, anodic polarization curves of the steel rod embedded in mortar was performed, using a saturated calomel electrode (SCE) as a reference electrode and the stainless steel mesh as a counter-electrode. The procedure was similar to that of the accelerated corrosion test: the specimens were placed in a plastic container with water for 72 h, and after that, the polarization curve started at a scan rate of 0.5 mV/s. Due to the low electrical conductivity of the system, the resistance between the steel rod and the reference electrode was determined in order to take into account the ohmic drop generated. The potentials were then converted into a standard hydrogen electrode (SHE) value.

3. Results

Fig. 2 shows a characteristic polarization curve of a steel rod embedded in mortar for specimen type (A). The same behaviour was found for both w/c ratio studied (0.5 and 0.6) and the two specimen sizes (30 mm and 71 mm in diameter). It can be seen that at potentials higher than the corrosion potential ($E_{corr} = -0.140\ V_{SHE}$), a passive region is observed with current densities of the order of 1 μA/cm^2. At potentials higher than 0.8 V_{SHE} the current density increases abruptly, probably due to a localized corrosion process and/or the evolution of oxygen due to water decomposition.

As for the accelerated corrosion test, Fig. 3 shows, as an example, the evolution of the potential between the steel rod and the stainless steel mesh necessary to kept the current density constant, for specimens type (A) and w/c = 0.6. The same behaviour was found in the 4 different condition studies: at low current densities, the potential remains low with slow increases along time, while for higher current densities, the potential increases abruptly and tends to stabilize. In some cases, a sudden decrease in the potential was observed. This was attributed to the cracking of the mortar: the presence of visible cracks let the water reach the steel rod decreasing the electrical resistivity of the media. In these cases, the tests were finished before the 15 days exposure time.

In general, specimens polarized at low current densities remained intact while specimens polarized at high current densities showed

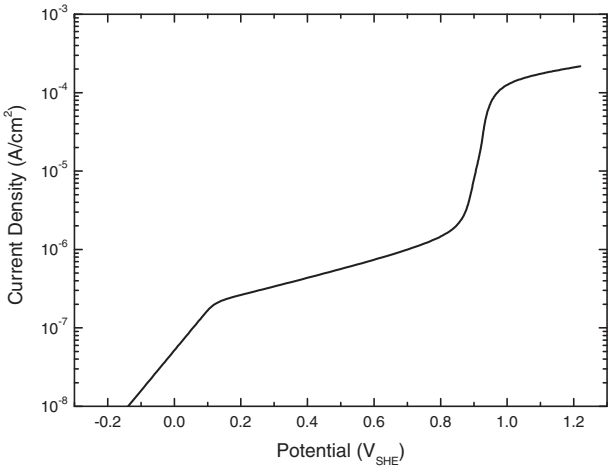

Fig. 2. Polarization curve of a steel bar embedded in mortar (specimen type A, w/c 0.6).

cracks radially distributed in the base and top of the specimens and parallel to the reinforcing bar (Fig. 4a and b).

After the accelerated corrosion tests, the mortar specimens were gamma-ray radiographiated. In the case of specimens tested at low current densities, no changes in the diameter of the rod were observed (Fig. 5a), while for high current densities, the presence of localized corrosion was detected (Fig. 5b), and the depth of this attack was detailed in Table 4.

Fig. 6 shows one of the steel bars extracted from the mortar specimen after the gamma-ray radiography. In this case, the mortar specimen was of the type A and the applied corrosion density was 750 μA/cm^2. It can be observed that the surface of the rebar is covered with orange or red-brown corrosion. SEM photographs from representative locations of the corroded steel bar are shown in Fig. 7. Fig. 7a shows magnetite with dense layered structure and clearly visible cracks. Cracks of this type are frequently found in magnetite layers [21–24]. The causes of the cracks are unknown, but their appearance (among other evidences) helps to identify the presence of magnetite. Fig. 7b shows a globular pattern, typical of *akaganeite*. Finally, in Fig. 7c, crystals in the form of fine plates ("flowery" structures), probably due to *lepidocrocite*, are observed. It is worth mentioning that the morphologies observed are similar to those reported by several authors [22–24].

The corrosion products can be easily flaked off with a razor blade. The rust so obtained reveals a mixture of black and red particles under

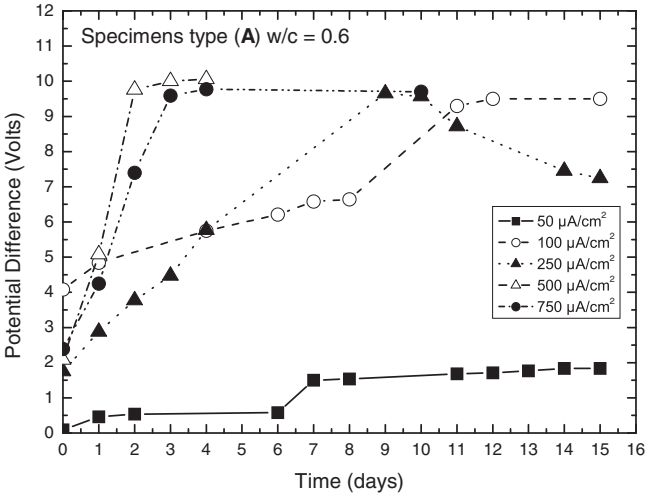

Fig. 3. Evolution of the potential difference between the steel rod and the stainless steel mesh as a function of time, for specimens with a w/c = 0.6 and 30 mm diameter.

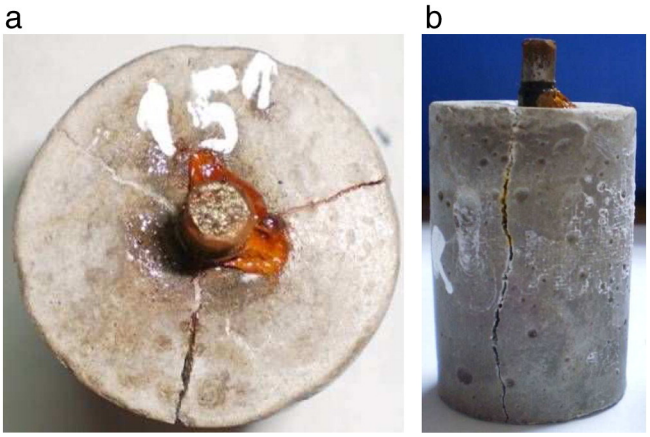

Fig. 4. Aspect of the mortar specimen after the accelerated corrosion test (specimen type A, w/c 0.6, $i_{app} = 250\ \mu A/cm^2$, t = 15 days).

low magnification. After a complete elimination of the corrosion products according to ASTM G1-90 standard [19], the naked bar was observed with the SEM (Fig. 8). In this case, the presence of, not only generalized corrosion but also localized corrosion in the form of pits is observed.

Table 4
Length of the localized attack (Lγ) determined by gamma-ray radiography, for specimens with different w/c ratios and diameters, and applied current densities.

w/c ratio	Mortar specimen type (diameter in mm)	I_{app} (μA/cm^2)	L_γ (μm)[a]
0.5	A (30)	250	205
			136
		500	253
		750	838
			746
	B (71)	250	122
			125
		500	291
			289
		750	784
			607
0.6	A (30)	250	376
			501
		500	184
			94
		750	203
	B (71)	100	104
			103
		750	202

[a] ±90 μm.

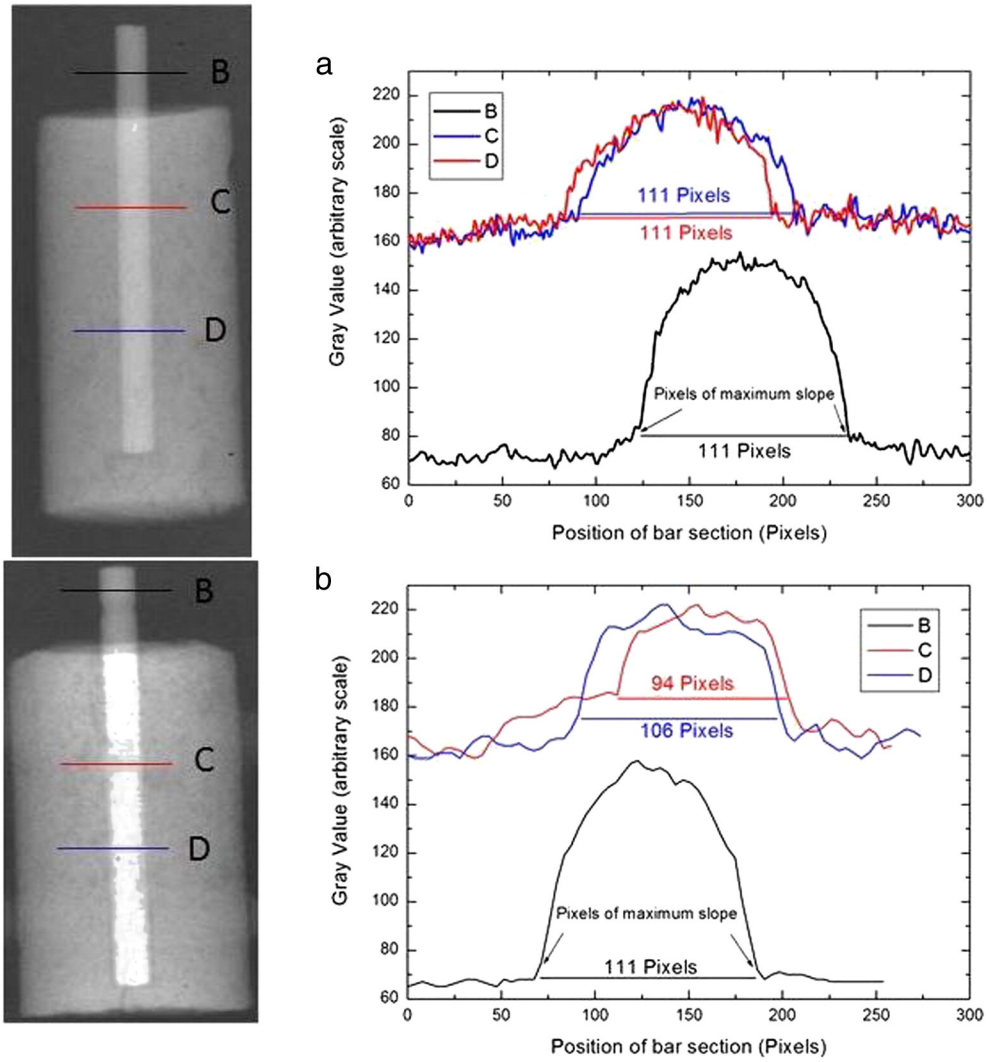

Fig. 5. Gamma-ray radiography of the specimens after the accelerated corrosion test. (a) Specimen type A, w/c 0.5, $i_{app} = 50\ \mu A/cm^2$, t = 15 days. (b) Specimen type A, w/c 0.5, $i_{app} = 750\ \mu A/cm^2$, t = 15 days.

Fig. 6. Optical microscope image of a steel bar after the extraction from the mortar specimen (specimen type A, w/c 0.6, $i_{app} = 750\ \mu A/cm^2$, t = 6 days).

Tables 5 to 8 show the weight loss of the steel bars after the accelerated corrosion tests, calculated with Eq. (2), for specimen types A and B and w/c 0.6 and 0.5. In the tables, the effective corrosion current density (calculated with Eq. (4)) as well as the length of the corrosion attack or the decreases in the rebar radio (L), assuming generalized corrosion, are also included. This last value was calculated with the following equation:

$$L = \frac{CR \cdot t}{\delta} \tag{5}$$

where δ is the density of the steel bars (7.87 g/cm^3).

In order to characterize the corrosion products generated during the accelerated corrosion tests, additional tests were performed and the corrosion products were scrapped and analysed with Mossbauer spectroscopy. Representative spectra are shown in Fig. 9. The occurrence of a mixture of Fe-bearing compounds was determined. At room temperature two doublets are the main components of the spectrum. The hyperfine parameters of one of them are: IS 0.38 mm/s and QS 0.58 mm/s. The other quadrupole doublet displays the following parameters: IS 0.37 mm/s and QS 0.99 mm/ s. These values are consistent to paramagnetic *akaganeite* which shows two different Fe^{3+} sites when chloride is present in the structure. It is worth noting that *akaganeite* is only stable in a chloride containing environment. However, such doublets are characteristic not only for *akaganeite* but also for other Fe^{3+}-bearing minerals. That is why we cannot rule out the presence of *lepidocrocite* (γ-FeOOH) and/or *ferrihydrite*. The spectrum took at 20 K confirms the presence of the compounds determined at room temperature. To sum-up, the main iron compounds detected with this technique were *akaganeite* and *lepidocrocite*, and in lower quantities intermediate *pirrotites*, *magnetite*, *maghemite*, *goethita* and *hematita*.

4. Discussion

Fig. 10 shows the polarization curves of a steel rebar embedded in mortar (specimen type A, w/c 0.6). In the same figure, the polarization curves reported by Nossoni and Harichandran [15], obtained for the same steel and in simulated pore solution (SPS) with and without chloride are shown. It can be observed that the behaviour of the steel embedded in mortar is similar to that immersed in SPS with chloride content between 0.032 and 0.31%: from the corrosion potential, a passive current is found with current densities of about 10^{-6} A/cm^2. This passive region ends at 0.85 V_{SHE}, where an abrupt increase of the current density is observed. This increment is attributed to the onset of a localized corrosion process, the evolution of oxygen from the solution, of both processes occurring simultaneously.

The occurrence of pitting was confirmed by SEM observations (Fig. 8). The species that induces pitting is the chloride present in the mortar. According to Table 1, the cement employed contains 0.06% chloride. Besides, the sand used also contains chloride ions (0.08%). So, taking into account the sand/cement ratio used in the mortar (s/c = 3), the final concentration of chloride in the mortar is 0.3%/cement. In spite of the fact that some discrepancies are found in literature concerning the threshold concentration of chloride to induce pitting in steel embedded in cementitious materials, this concentration is enough to induce localized corrosion [25–27].

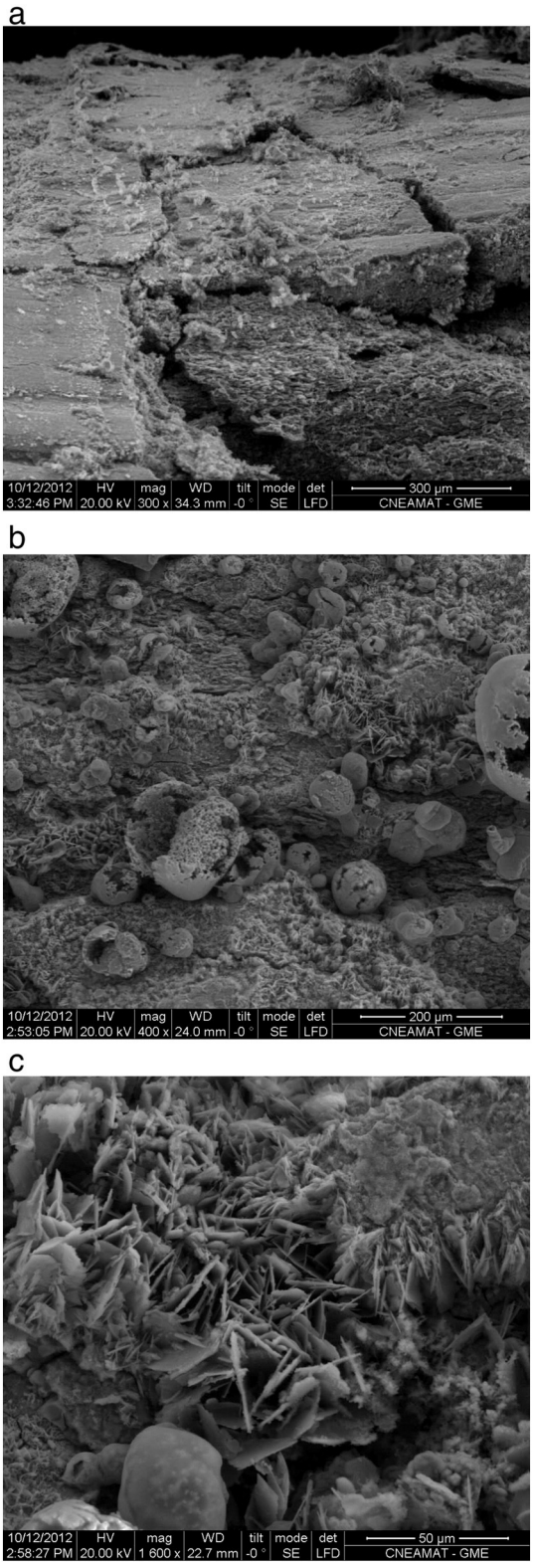

Fig. 7. SEM images of the corrosion products formed on the steel bar during the accelerated corrosion test (specimen type A, w/c 0.6, $i_{app} = 750\ \mu A/cm^2$, t = 6 days).

Although the results obtained in the mortar and in SPS cannot be directly compared, a concentration of 0.3% chloride/cement seems to be equivalent to a concentration of 0.31% in SPS, as shown in Fig. 10. This value will be taken into account to justify the occurrence of localized corrosion in the present work.

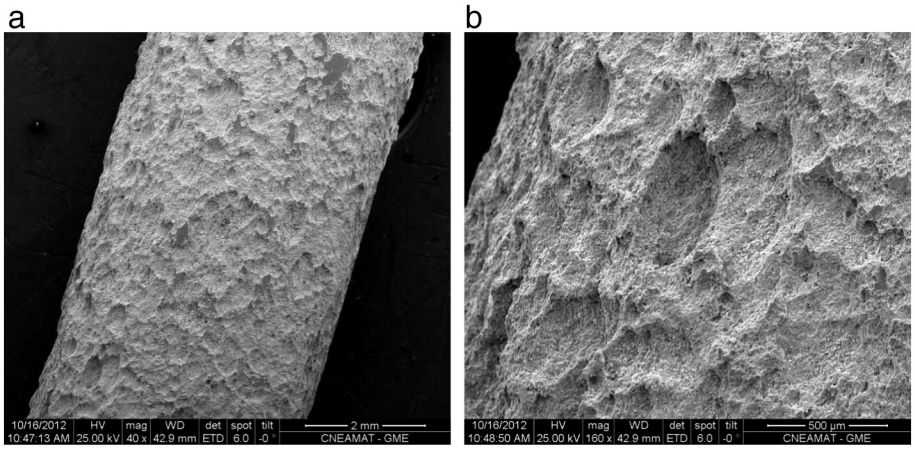

Fig. 8. SEM images of a steel bar after the elimination of the corrosion products (specimen type A, w/c 0.6, $i_{app} = 750\ \mu A/cm^2$, t = 6 days).

The Pourbaix diagram for the system Fe/H_2O [28] shows that at the pH of a typical mortar (about 13), it exists only two regions: immunity and passivity. However, taking into account the "modified" Pourbaix diagram with the presence of 0.3% chloride [28,29] (Fig. 11), pits only appears at potential equal or higher than the *pitting potential*, but existing pits can grow even at lower potentials. Those pits stop growing only at potential lower than the called *repassivation potential* (or *protection potential*). This is why, the passivity region in the Fe/H_2O diagram splits in 3 regions in the $Fe/Cl^-/H_2O$ diagram: pitting region, with a lower limit given by the *pitting potential*, imperfect passivity region, limited by the *pitting potential* (higher limit) and the *repassivation potential* (lower limit), and the perfect passivation region, limited by *repassivation potential* (higher limit) and the thermodynamic potential of the passive layer formation.

In Fig. 11 it can be concluded that, from the experimental conditions employed in the present work (a mortar with chloride content than can be simulated by 0.3% chloride in SPS) and, at the potentials needed to induce accelerated corrosion (higher than 0.8 V_{SHE}), the steel should undergo pitting. This explains why SEM observations as well as with gamma-ray radiography reveal the existence of pitting. Even more, the occurrence of *akaganeite* as the main corrosion product (determined microscopically and with TMS) is a clear indication of the presence of chloride ions as responsible of the corrosive process found.

As for the efficiency of the corrosion current density, Fig. 12 shows the results obtained for specimens A and B, and for w/c ratio equal to 0.5 and 0.6.

The first observation that arises in Fig. 12 is the lack of reproducibility of the result for certain experimental conditions. This fact has also been reported by several authors [8,15]. For specimen type A (lower diameter), no matter the w/c ratio employed, the efficiency of the current density lies between 1 and 77%, and the efficiency is independent of the applied current density. On the other hand, for specimen type B (higher diameter), the efficiency is a function of the applied current density: the higher the current density, the higher the efficiency. In this case, the efficiency lies between 1 and 45%. The fact that, in all cases, the efficiency is lower than 100% is indicative of the fact that only a part of the applied current density is consumed in the oxidation of the metal and that another anodic process consumes the remaining of the applied current. This low efficiency has been reported by Nossoni and Harichandran [15] who observed that the efficiency was dependent of the applied current density and of the chloride content. Fig. 13 shows the efficiency reports by these authors as compared to those obtained in the present work for a similar applied current density. It can be observed that for specimens with the lower w/c ratio (0.5), the values are similar to those reported by Nossoni and Harichandran [15], while for the higher w/c ratio (0.6), the efficiency is lower.

Caré and Raharinaivo [13] reported that in accelerated corrosion tests, the steel corrosion obeys Faraday's law only in highly chlorated media (with current efficiencies in some cases higher that 100%) revealing that the main anodic process in the dissolution of the steel. On the contrary, in test without chloride or with lower content of this ion (as is the case of the present work), they propose that the accelerated corrosion is a very complex process with low efficiencies. Nossoni and Harichandran [15] postulate that for low chloride contents, Faraday's law cannot predict accurately the weight loss of the steel because there are competitive reactions in the anode, that depend on the chloride concentration of the system, pH of the solution and applied current densities. The main competitive reaction to the steel dissolution is oxygen evolution from the decomposition of the solution according to:

$$4OH^- \rightarrow O_2 + 2H_2O + 4e^-.$$

Another possibility to explain the low current efficiency found is the fact that iron oxidation led to Fe(III) instead of Fe(II), as proposed by

Table 5
Corrosion rate (CR), length of the corrosion attack (L) and effective current density (i_{eff}) as a function of the applied current density (i_{app}) for a type specimens and w/c = 0.6.

i_{app} ($\mu A/cm^2$)	CR ($g/cm^2 * year$)	L (μm)	i_{eff} ($\mu A/cm^2$)
50	0.0130 ± 0.0005	1.36 ± 0.03	1.4 ± 0.1
50	0.0084 ± 0.0005	0.87 ± 0.03	0.9 ± 0.1
100	0.0213 ± 0.0006	3.51 ± 0.03	2.3 ± 0.1
100	0.0337 ± 0.0006	2.22 ± 0.03	3.7 ± 0.1
250	1.2322 ± 0.0034	128.68 ± 0.18	135.0 ± 0.4
250	1.7483 ± 0.0046	182.58 ± 0.24	191.6 ± 0.5
500	0.5175 ± 0.0017	54.05 ± 0.09	56.7 ± 0.2
500	0.5232 ± 0.0020	38.24 ± 0.07	57.3 ± 0.2
750	0.3541 ± 0.0052	4.38 ± 0.03	38.8 ± 0.6
750	0.6378 ± 0.0034	18.13 ± 0.05	69.9 ± 0.4
750	0.7591 ± 0.0024	63.42 ± 0.10	83.2 ± 0.3

Table 6
Corrosion rate (CR), length of the corrosion attack (L) and effective current density (i_{eff}) as a function of the applied current density (iapp) for b type specimens and w/c = 0.6.

i_{app} ($\mu A/cm^2$)	CR ($g/cm^2 * year$)	L (μm)	i_{eff} ($\mu A/cm^2$)
50	0.0064 ± 0.0006	0.64 ± 0.03	0.7 ± 0.1
50	0.0084 ± 0.0005	0.86 ± 0.03	0.9 ± 0.1
100	0.0805 ± 0.0007	8.06 ± 0.04	8.8 ± 0.1
100	0.1127 ± 0.0008	11.05 ± 0.04	12.3 ± 0.1
250	0.0824 ± 0.0007	8.25 ± 0.04	9.0 ± 0.1
250	0.0225 ± 0.0006	2.21 ± 0.03	2.5 ± 0.1
500	0.4664 ± 0.0018	35.99 ± 0.07	51.1 ± 0.2
500	0.3486 ± 0.0016	24.77 ± 0.06	38.2 ± 0.2
750	0.7501 ± 0.0029	36.56 ± 0.07	82.2 ± 0.3
750	2.2319 ± 0.0058	196.83 ± 0.26	244.6 ± 0.6

Table 7
Corrosion rate (CR), length of the corrosion attack (L) and effective current density (i_{eff}) as a function of the applied current density (iapp) for a type specimens and w/c = 0.5.

i_{app} ($\mu A/cm^2$)	CR ($g/cm^2 * year$)	L (μm)	i_{eff} ($\mu A/cm^2$)
50	0.0095 ± 0.0005	0.99 ± 0.03	1.0 ± 0.1
50	0.0160 ± 0.0006	1.67 ± 0.03	1.7 ± 0.1
100	0.0092 ± 0.0005	0.97 ± 0.03	1.0 ± 0.1
100	0.0108 ± 0.0005	1.13 ± 0.03	1.2 ± 0.6
250	0.6015 ± 0.0019	62.82 ± 0.10	65.9 ± 0.2
250	0.2220 ± 0.0010	23.18 ± 0.05	24.3 ± 0.1
500	0.7605 ± 0.0023	79.42 ± 0.12	83.3 ± 0.1
500	0.2404 ± 0.0013	17.78 ± 0.05	26.3 ± 0.1
750	3.2158 ± 0.0080	320.00 ± 0.40	352.4 ± 0.9
750	3.2677 ± 0.0082	281.55 ± 0.36	358.1 ± 0.9

Table 8
Corrosion rate (CR), length of the corrosion attack (L) and effective current density (i_{eff}) as a function of the applied current density (iapp) for b type specimens and w/c = 0.5.

i_{app} ($\mu A/cm^2$)	CR ($g/cm^2 * year$)	L (μm)	i_{eff} ($\mu A/cm^2$)
50	0.0255 ± 0.0006	2.64 ± 0.03	2.8 ± 0.1
50	0.0150 ± 0.0006	1.56 ± 0.03	1.6 ± 0.1
100	0.0152 ± 0.0006	1.58 ± 0.03	1.7 ± 0.1
100	0.0100 ± 0.0005	1.05 ± 0.03	1.1 ± 0.1
250	0.1768 ± 0.0009	18.46 ± 0.05	19.4 ± 0.1
250	0.3085 ± 0.0012	32.22 ± 0.06	33.8 ± 0.1
500	1.2831 ± 0.0035	130.39 ± 0.18	140.6 ± 0.4
500	1.2196 ± 0.0034	127.37 ± 0.18	133.6 ± 0.4
750	3.0519 ± 0.0076	318.73 ± 0.40	334.4 ± 0.8
750	2.8949 ± 0.0073	302.33 ± 0.38	317.2 ± 0.8

Nossoni and Harichandran [15]. These authors also postulate that for high chloride concentration and when there is no limitation of water in the system, the efficiency is close to 100%. So, the Faraday's law can be applied to accurately predict the weight loss of the steel only when the applied current density is not very high. On the other hand, some results suggest that when physical barriers restrict the diffusion of water and chloride into concrete, Faraday's law is not expected to yield an accurate estimate of the mass loss in accelerated corrosion tests of concrete specimens.

On the other hand, when an electric field is applied to induce accelerated corrosion, the water electrolysis is produced in both electrodes: working electrode (steel bar) and counter-electrode (stainless steel mesh). In these conditions, the oxygen evolution in the working electrode is due to the consumption of OH^- and a decrease in the pH is generated in the vicinity of the steel bar. So, even in the absence of chloride ions, the decrease in the pH value can generate a situation where it is impossible for the steel bar to keep in the passive state. This leads to localized corrosion even though the chloride content of the mortar is below the threshold value to induce corrosion in natural conditions.

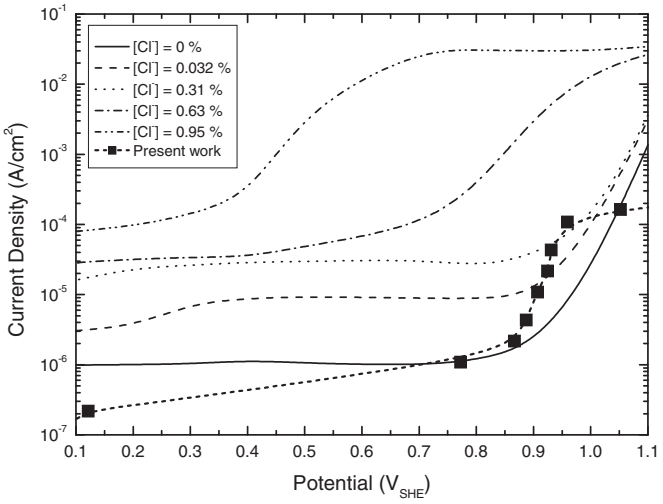

Fig. 10. Polarization curve of a steel bar embedded in mortar as compared with those published by [15], obtained in simulated pore solution (SPS).

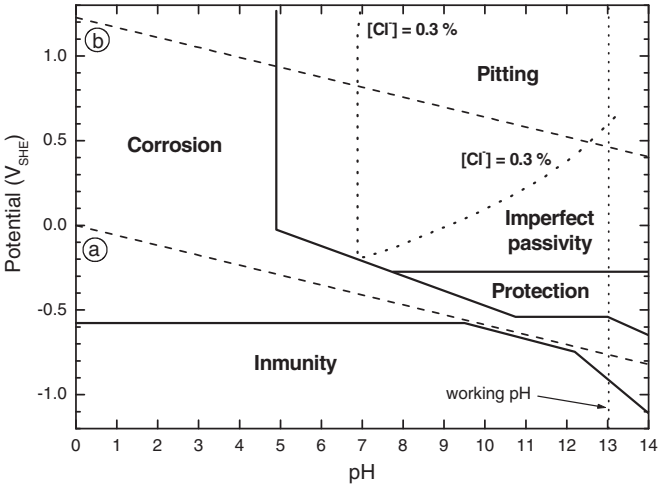

Fig. 11. Potential-pH diagram for the Fe–Cl^-–H_2O system, for a chloride concentration equal to 0.3%, at 25 °C.

As mentioned by González et al. [7], the usual practice of applying a constant anodic current to reinforcements to measure the time-to-fracture or to determine the relation between the corrosive attack and the time-to-cracking via Faraday's law leads to uncertain results

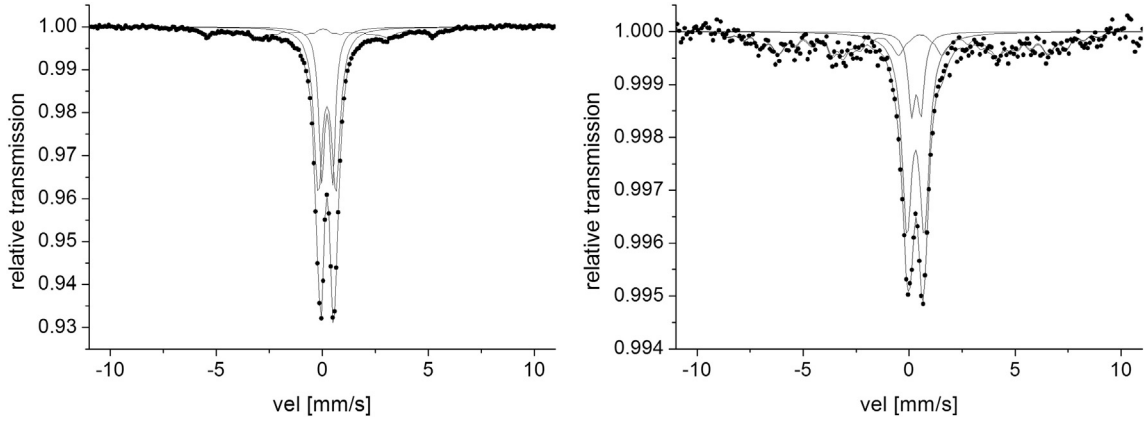

Fig. 9. TMS of the corrosion products obtained (specimen type A, w/c 0.6, i_{app} = 750 $\mu A/cm^2$, t = 6 days). Left: spectra obtained at room temperature, right: spectra obtained at 20 K.

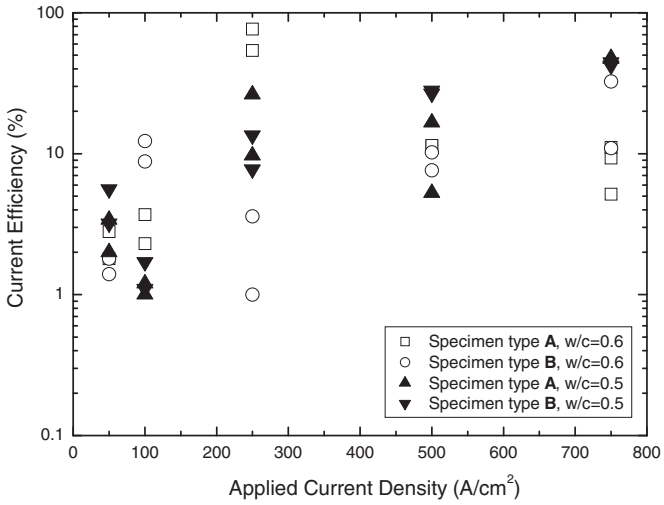

Fig. 12. Current efficiency as a function of the applied current density, cover mortar depth and water/cement ratio.

because of the several parameters involved. Apart from the specific volume of solid corrosion products generated during tests, cracking is influenced by other factors. Among them, the mains are: (a) the rate of Fe(II) ion formation; (b) the diffusion of Fe(II) to the outside; (c) the solubility of corrosion products, and (d) the chemical composition of the aqueous phase in the pores. All of these factors are mutually dependent. Besides, the relationship between the extension of the corrosion attack and the time-to-cracking depends on additional factors, such as: (e) current efficiencies higher than 100%, (f) non-uniform penetration of corrosion in corroded areas, with pits that overlapped with a generalized attack, and (g) preferential transport of corrosion products to generate rust spots on the surface. Then, in spite of the fact the during the accelerated corrosion test a uniform current density is applied, not only uniform attack but also localized attack is obtained. This lead to the conclusion that it is very difficult to estimate the time-to-cracking from data obtained from accelerated corrosion tests.

As for the gamma-ray radiography tests performed, in the experimental conditions employed in the present work, the detection limit is of the order of 90 μm. It was not possible to determine the length of the generalized corrosion but, the occurrence of pitting allowed employing this technique to measure the depth of the pits. Fig. 14 shows the length of the corrosive attack calculated from the weight

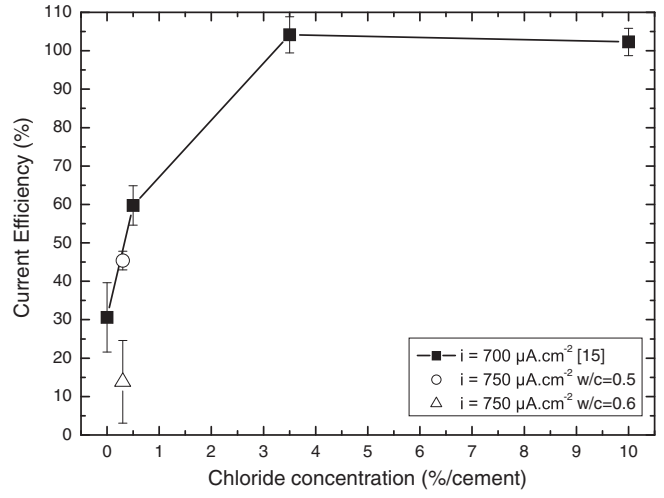

Fig. 13. Current efficiency obtained in the present work as compared with those published by [15] in similar conditions.

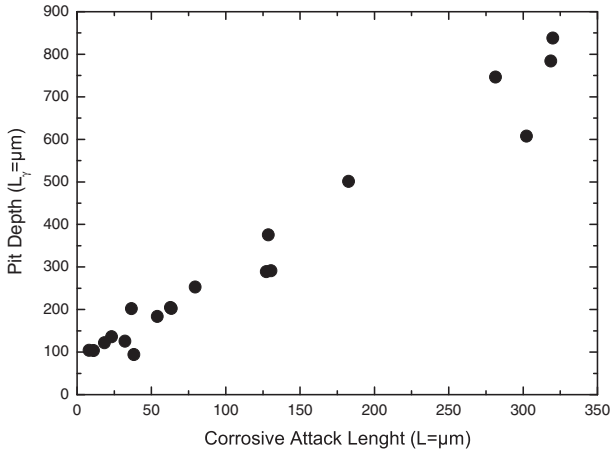

Fig. 14. Pit depth measured with gamma-ray radiography as a function of the corrosive attack length calculated from weight loss tests assuming uniform corrosion.

loss data (assuming generalize corrosion) and the depth of the deepest pit measured with gamma-ray radiography. The correlation has a slope close to 3. This means that the depth of the localized attack is about 3 times the predicted length of the attack assuming uniform corrosion. These results are consistent with the findings of Gonzalez et al. [30] who reported that the maximum penetration of localized attack on steel embedded in concrete containing chlorides is equivalent to about four to eight times the average general penetration predicted with electrochemical techniques.

5. Conclusions

From the present work, the following conclusions can be drawn:

- In the experimental conditions used in the present work, the accelerated corrosion of steel bars embedded in mortar has a current density efficiency much lower than 100% due to the occurrence of an anodic reaction different from that of iron dissolution. This reaction is probably the oxygen evolution. On the other hand, the efficiency is not related to the applied current density, the water/cement ratio or the mortar cover depth of the embedded steel.
- The main corrosion product generated during the accelerated test is *akaganeite* (β-FeOOH). This fact, plus the occurrence of pits on the steel surface is consistent with the chloride content of the mortar.
- The gamma-ray radiography has a detection limit (in the experimental conditions of the present work) equal to 90 μm and was successfully used to determine the depth of the pit generated.
- The relationship between the maximum depth of the localized corrosion and the length of the uniform attack obtained from weight loss measurements is close to 3, consistent with previous reported works.

Acknowledgements

The financial support of the CONICET (Consejo Nacional de Investigaciones Científicas y Técnicas), the Universidad Nacional de San Martín (UNSAM) (800x600 PROG07A/1) and of the FONCYT (PICT 2008/2216), Secretaría para la Tecnología, la Ciencia y la Innovación Productiva, Argentina, is acknowledged.

References

[1] J.P. Broomfield, Corrosion of Steel in Concrete: Understanding, Investigation and Repair, E&FN SPON, London/New York, 1997.
[2] A. Bentur, S. Diamond, N.S. Berke, Steel Corrosion in Concrete: Fundamentals and Civil Engineering Practise, Taylor & Francis, London, 1997.

[3] P. Pedeferri, B. Polder, L. Bertolini, B. Elsener, Corrosion of Steel in Concrete: Prevention, Diagnosis, Repair, Wiley-VCH, Weinheim, 2004.
[4] M. Murat, M. Charbonnier, A. Ahmadi Hachemi, J.C. Cubaud, Nature particuliere des oxydes de fer hydrates formes dans certaines conditions de corrosion acceleree de l'acier dans le beton armee, Cem. Concr. Res. 4 (1974) 945–952.
[5] C. Andrade, C. Alonso, F.J. Molina, Cover cracking as a function of bar corrosion: part I — experimental tests, Mater. Struct. 26 (1993) 453–464.
[6] J.G. Cabrera, Deterioration of concrete due to reinforcement steel corrosion, Cem. Concr. Compos. 18 (1996) 47–59.
[7] J.A. González, S. Feliu, P. Rodríguez, Threshold steel corrosion rates for durability problems in reinforced structures, Corrosion 53 (1997) 65–71.
[8] T. El Maaddawy, K. Soudky, Effectiveness of impressed current technique to simulate corrosion of steel reinforcement in concrete, J. Mater. Civ. Eng. 15 (2003) 41–47.
[9] A.A. Torres-Acosta, M.J. Fabela-Gallegos, A. Muñoz-Noval, D. Vázquez-Vega, J.R. Hernandez-Jimenez, M. Martínez-Madrid, Influence of corrosion on the structural stiffness of reinforced concrete beams, Corrosion 60 (2004) 862–872.
[10] S.A. Austin, R. Lyons, M.J. Ing, Electrochemical behavior of steel-reinforced concrete during accelerated corrosion testing, Corrosion 60 (2004) 203–214.
[11] B. Assoulia, F. Simescua, G. Debickib, H. Idrissi, Detection and identification of concrete cracking during corrosion of reinforced concrete by acoustic emission coupled to the electrochemical techniques, NDT&E Int. 38 (2005) 682–689.
[12] M. Ing, S. Austin, R. Lyons, Cover zone properties influencing acoustic emission due to corrosion, Cem. Concr. Res. 35 (2005) 284–295.
[13] S. Caré, A. Raharinaivo, Influence of impressed current on the initiation of image in reinforced mortar due to corrosion of embedded steel, Cem. Concr. Res. 37 (2007) 1598–1612.
[14] S. Caré, Q.T. Nguyen, V. L'Hostis, Y. Berthaud, Mechanical properties of the rust layer induced by impressed current method in reinforced mortar, Cem. Concr. Res. 38 (2008) 1079–1091.
[15] G. Nossoni, R. Harichandran, Current efficiency in accelerated corrosion testing of concrete, Corrosion 68 (2012) 801–809.
[16] M.A.J. Mariscotti, P. Thieberger, T. Frigerio, F. Mariscotti, M. Ruffolo, Investigations with reinforced concrete tomography, Structural Faults & Repairs 2008, in: M.C. Forde (Ed.), 12th International Conference, Engineering Technics Press, Edinburgh, 2008.
[17] D.M. McCann, M.C. Forde, Review of NDT methods in the assessment of concrete and masonry structures, NDT&E Int. 34 (2001) 71–84.
[18] ASTM, Standard C 305-99, standard practice for mechanical mixing of hydraulic cement pastes and mortars of plastic consistency, Annual Book of ASTM Standard, vol. 04.01, ASTM, West Conshohokem, PA, 2004.
[19] ASTM, G 1-03, standard practice for preparing, cleaning and evaluating corrosion test specimens, Annual Book of ASTM Standard, vol. 03.02, ASTM, West Conshohokem, PA, 2004.
[20] R.A. Brandt, Normos Program, Forschungszentrum Julich GmbH (KFA), Julich, Germany, 1989.
[21] G.S. Duffó, W. Morris, I. Raspini, C. Saragovi, A study of rebars embedded in concrete during 65 years, Corros. Sci. 46 (2004) 2143–2157.
[22] A. Razvan, A. Raman, Morphology of rust phases formed on naturally weathered weathering steel in bridge span, Prakt. Metallogr. 23 (1986) 223–236.
[23] A. Raman, S. Nasrazadani, L. Sharma, Morphology of rust phases formed on weathering steels in various laboratory corrosion tests, Metallography 22 (1989) 79–96.
[24] D. de la Fuente, I. Díaz, J. Simancas, B. Chico, M. Morcillo, Long-term atmospheric corrosion of mild steel, Corros. Sci. 53 (2011) 604–617.
[25] M. Manera, Ø. Vennestand, L. Bertolini, Chloride threshold for rebar corrosion in concrete with addition of silica fume, Corros. Sci. 50 (2008) 554–560.
[26] U. Angst, B. Elsener, C. Larsen, Ø. Vennesland, Critical chloride content in reinforced concrete — a review, Cem. Concr. Res. 39 (2009) 1122–1138.
[27] K.Y. Ann, H.W. Song, Chloride threshold level for corrosion of steel in concrete, Corros. Sci. 49 (2007) 4113–4133.
[28] M. Pourbaix, Applications of electrochemistry in corrosion science and in practice, Corros. Sci. 14 (1974) 25–82.
[29] M. Moreno, W. Morris, M.G. Alvarez, G.S. Duffó, Corrosion of reinforcing steel in simulated concrete pore solutions. Effect of carbonation and chloride content, Corros. Sci. 46 (2004) 2681–2699.
[30] J.A. González, C. Andrade, C. Alonso, S. Feliu, Comparison of rates of general corrosion and maximum pitting penetration of concrete embedded steel reinforcement, Cem. Concr. Res. 25 (1995) 257–264.